

In Situ Observation of the Surface Processes Involved in Dissolution from the (010) Surface of Potassium Ferrocyanide Trihydrate in Aqueous Solution Using an Integrated Electrochemical–Atomic Force Microscope

Claire E. Jones, Julie V. Macpherson,* and Patrick R. Unwin*

Department of Chemistry, University of Warwick, Coventry, CV4 7AL, U.K.

Received: October 5, 1999; In Final Form: December 2, 1999

The surface processes accompanying dissolution from the (010) surface of potassium ferrocyanide trihydrate in aqueous solution have been determined using an integrated electrochemical–atomic force microscope (IE-AFM). This instrument employs a Pt-coated AFM tip that functions as an electrode, as well as a conventional topographical imaging device. The dissolution process was induced by oxidizing ferrocyanide at the tip, from an initially saturated solution, thereby creating a local undersaturation at the crystal–solution interface. The subsequent dissolution behavior was imaged in real time as a function of the diffusional driving force. At low driving force, the dissolution process proceeds mainly by the retreat of preexisting steps aligned in the dominant [102] direction. With increasing driving force, dissolution occurs via the unwinding of steps from screw dislocation sites, leading to the formation of macroscopic etch pits, with an outline morphology determined by the [102] and [201] directions. At the highest driving forces the density of etch pits corresponds closely with the observed density of growth hillocks on the crystal surface, prior to dissolution. The surface dynamics observed under diffusion-controlled conditions are consistent with earlier scanning electrochemical microscopy kinetic studies (Macpherson, J. V.; Unwin, P. R. *J. Phys. Chem.* **1995**, *99*, 3338) which interpreted the process in terms of the classical Burton, Cabrera, and Frank dissolution model.

Introduction

The growth and dissolution behavior of crystalline solids has been extensively studied^{1,2} for fundamental interest and also because these processes are of key importance in many natural,³ technological,⁴ and biological processes.⁵ With the advent of scanned probe microscopes (SPMs),⁶ unprecedented structural information has been obtained on the elementary steps involved in these processes,^{7–9} particularly on the roles of elementary features such as kinks, steps, and dislocations.¹⁰ In particular, atomic force microscopy (AFM) has provided evidence for the operation of the classical Burton, Cabrera, and Frank (BCF) model¹¹ in the growth of crystal surfaces.^{12–19} This model, which treats the growth process in terms of the movement of monatomic steps, has been widely used to interpret growth (and dissolution) kinetics at the solid–liquid interface.^{1,2}

The scanning electrochemical microscope (SECM)²⁰ has proven powerful for investigating the dissolution kinetics of ionic single-crystal surfaces.^{21–23} With this methodology, a tiny electrode (of micrometer dimensions) placed close to a crystal surface in solution, is used to amperometrically drive and monitor the phase transfer dynamics, by creating a local undersaturation at the interface of interest. The technique offers several attributes including well-defined, variable and calculable mass transfer, enabling a wide range of reaction rates to be interpreted in terms of interfacial concentrations. For systems characterized by rapid dissolution kinetics, we have demonstrated that the rate laws determined by SECM were consistent with BCF theory.^{21b,c,22,23} A limitation of the SECM approach, however, was that most complementary topographical information was at the micrometer scale, either ex situ using optical microscopy^{21b,22} or in situ using SECM operating in the negative feedback mode.^{22,24} This level of resolution is clearly incompat-

ible with that required to assess structurally the applicability of the BCF model.

Together with Hillier and Bard, we have recently made progress toward combining SECM and AFM, to enable dissolution to be initiated electrochemically and the resulting surface processes monitored in situ.²⁵ By employing Pt-coated AFM probes, insulated at all but the cantilever and the tip, electrolysis at the probe was employed to induce dissolution from the (100) cleavage plane of a single crystal of potassium bromide in acetonitrile solution, and the evolving topography of the sample was imaged in response to the perturbation.²⁵ Using this integrated electrochemical–AFM (IE-AFM) approach, the first in situ experimental evidence was obtained for the operation of the spiral (BCF) mechanism in the dissolution of an ionic single crystal. In these studies, steps of unit cell height were imaged dynamically, unwinding from screw dislocations emerging on the crystal surface.

In this paper, we use the IE-AFM to identify the surface processes involved in dissolution from the (010) surface of a single crystal of potassium ferrocyanide trihydrate. The kinetics for this process have been shown to be rapid by SECM and to conform to the BCF dissolution model.²² This system therefore represents an ideal test candidate for assessing the applicability of the BCF model in describing fast dissolution processes.

Experimental Section

Materials. All solutions were prepared with Milli-Q reagent water (Millipore Corp). Saturated potassium ferrocyanide trihydrate ($K_4Fe(CN)_6 \cdot 3H_2O$; Fisher-Scientific, A.R.) solutions were prepared by first making up 3.5 mol dm⁻³ potassium chloride (BDH, A.R. grade) and then adding potassium ferrocyanide trihydrate until the solution became saturated. The high

concentration of potassium chloride served as a supporting electrolyte and maintained the total potassium concentration at an essentially constant value during the electrochemically induced dissolution process. The saturated concentration of $\text{Fe}(\text{CN})_6^{4-}$ in the 3.5 mol dm^{-3} KCl solution was determined as $0.133 \text{ mol dm}^{-3}$ by measuring the steady-state transport-limited current for the oxidation of $\text{Fe}(\text{CN})_6^{4-}$ at a $25 \mu\text{m}$ diameter Pt ultramicroelectrode (UME). The diffusion coefficient for $\text{Fe}(\text{CN})_6^{4-}$ under identical solution conditions has been measured previously as $5.5 \times 10^{-6} \text{ cm}^2 \text{ s}^{-1}$.²²

Potassium ferrocyanide trihydrate crystals were grown from seeds in saturated aqueous solutions through slow evaporation.²² Slow growth over 9–10 weeks yielded well-defined monoclinic (tabular) crystals with an average length of 1.2 cm. Visual inspection of crystal surfaces before and after IE-AFM experiments was carried out with an Olympus BH2 light microscope, equipped with a 3-CCD color video camera system (JVC, model KY-F55BE). The camera was linked to a video capture card (Image Grabber/PCI, Neotech) that allowed images to be transferred to a PC. The crystal morphology, and the face of interest, was identified by measuring the interfacial angles of the exposed faces directly from micrographs.

Integrated Electrochemical–AFM Instrumentation. IE-AFM experiments employed a Nanoscope E AFM and fluid cell (Digital Instruments, Santa Barbara, CA). The AFM was equipped with a sample scanner that facilitated a maximum scan range of $120 \mu\text{m} \times 120 \mu\text{m}$, with images typically recorded at either $87.7 \mu\text{m} \times 87.7 \mu\text{m}$ (low resolution) or $20 \mu\text{m} \times 20 \mu\text{m}$ (higher resolution). All images were acquired using the contact mode of operation, under constant force conditions with 256 lines per scan. The tip–sample force was minimized just before imaging by reducing the set point to a value just prior to tip disengagement. AFM probes (Nanoprobes, Digital Instruments) consisted of silicon nitride cantilevers (length $100 \mu\text{m}$: spring constant 0.38 N m^{-1}) with integrated pyramidal tips, that had a height of $2.86 \mu\text{m}$ and a base width of $4 \mu\text{m}$. For IE-AFM studies, the underside of the probe was sputter coated, initially with Cr (3 nm), and then with Pt (60 nm), as described previously,^{25,26} to provide a conducting AFM tip capable of functioning as an electrode, as well as a force sensor. This procedure has been carefully optimized²⁶ to produce metal-coated probes that are (i) durable, (ii) long-lasting, and (iii) coated evenly with Pt, to the very end of the tip.

The probe was secured in place in the fluid cell and the underside coated in a 2:1 (by volume) solution of adhesive (Super Glue, UK) and nail varnish (Miners International Ltd., Andover, UK), using a fine paintbrush. This procedure served to insulate electrically the part of the probe holder that came into contact with the solution and most of the area of the AFM chip adjacent to the cantilever and the tip. The coating was allowed to dry in air for 60 min. Electrical contact was made to the cantilever via the metal spring clasp of the fluid cell probe holder, external to the cell.

Electrochemical control of the AFM probe was achieved in a three-electrode mode, using a model EI-400 bipotentiostat (Cypress Systems, USA) with an external voltage source provided by a waveform generator (Colburn Electronics, Coventry, UK). Current–potential characteristics were recorded on a PC equipped with a data acquisition card (Lab-PC-1200, National Instruments Corp. Ltd., UK) using software written in-house by Mr. N. J. Evans. The Pt-coated AFM probe served as the working electrode, with a silver wire functioning as a quasi-reference electrode (AgQRE) and a Pt wire acting as a counter electrode. The latter two electrodes were secured in

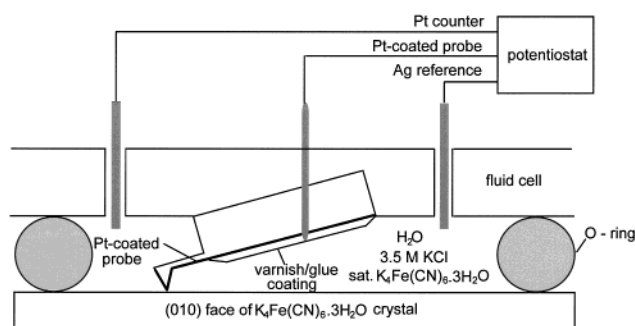


Figure 1. Schematic of the IE-AFM probe employed in the fluid cell.

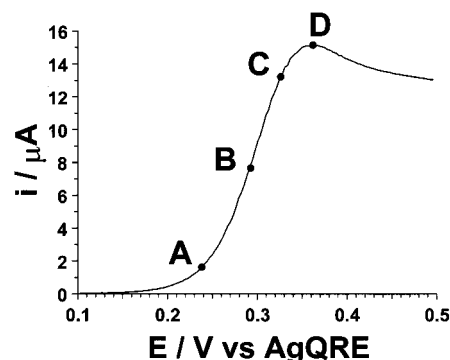


Figure 2. Current–voltage characteristics recorded at an IE-AFM probe for the oxidation of $\text{Fe}(\text{CN})_6^{4-}$ in a 3.5 mol dm^{-3} KCl solution saturated with respect to $\text{K}_4\text{Fe}(\text{CN})_6 \cdot 3\text{H}_2\text{O}$. The potential scan rate was 10 mV s^{-1} . The potentials to which the probe was pulsed during electrochemically induced AFM dissolution studies are labeled A–D.

place in the outlet ports of the fluid cell. A schematic of the experimental arrangement is shown in Figure 1.

All IE-AFM images were acquired using a sample scan rate of 6.10 Hz; enabling images to be captured every 42 s, after electrochemical induction of the dissolution process.

Results and Discussion

Electrochemical Characteristics of the IE-AFM Probe. A typical linear sweep voltammogram, recorded at a potential scan rate of 10 mV s^{-1} , for the oxidation of $\text{Fe}(\text{CN})_6^{4-}$ to $\text{Fe}(\text{CN})_6^{3-}$ at an IE-AFM probe, in a solution containing 3.5 mol dm^{-3} KCl, saturated with respect to potassium ferrocyanide trihydrate, is shown in Figure 2. Assuming a linear diffusion profile and a reversible electron transfer process, the value for the exposed electroactive area, A , was determined using eq 1²⁷

$$A = \frac{i_p}{(2.69 \times 10^5)n^{3/2}D^{1/2}\nu^{1/2}c^*} \quad (1)$$

where n is the number of electrons transferred per redox event ($n = 1$), D and c^* are the diffusion coefficient and concentration of the electroactive species of interest, i_p is the magnitude of the peak current, and ν is the potential scan rate. For the saturated $\text{Fe}(\text{CN})_6^{4-}$ system, $D = 5.5 \times 10^{-6} \text{ cm}^2 \text{ s}^{-1}$, $c^* = 0.133 \text{ mol dm}^{-3}$, and $i_p = 15.2 \mu\text{A}$, giving a value of $A = 0.2 \text{ mm}^2$. This result was typical for the probes employed in the dissolution experiments described herein. Given the geometry of the IE-AFM probe, it should be noted that this calculation overestimates the true exposed electrode area, as enhanced diffusional effects at the edges of the cantilever and the tip are unaccounted for.

This voltammetric measurement was made with the tip retracted sufficiently far from the surface of the underlying

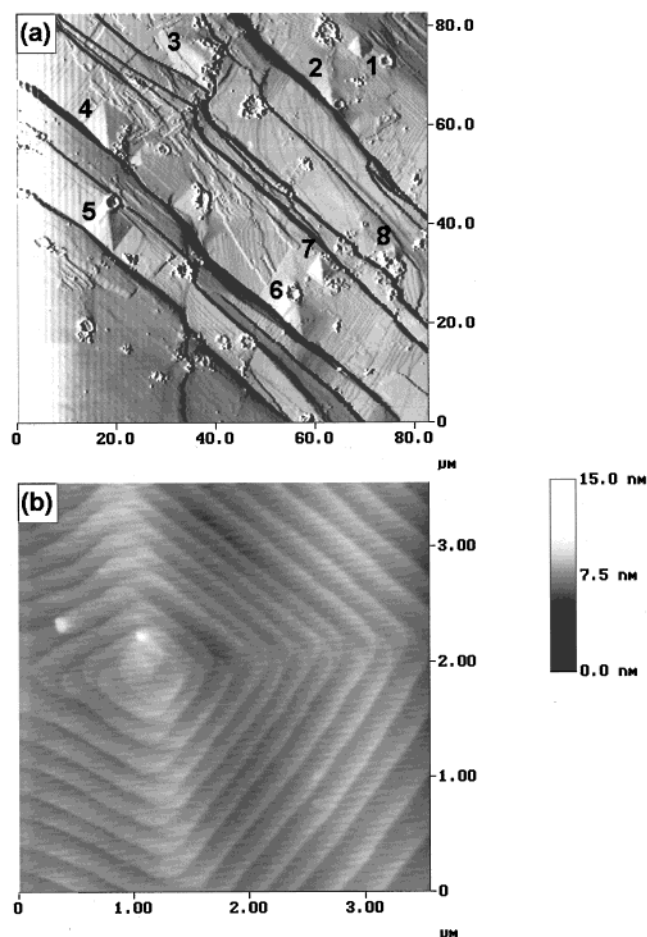


Figure 3. In air AFM images of the (010) surface of potassium ferrocyanide trihydrate: (a) $82.5\ \mu\text{m} \times 82.5\ \mu\text{m}$ deflection image recorded at a scan rate of 8.15 Hz. The presence of eight growth spirals is indicated; (b) $3.6\ \mu\text{m} \times 3.6\ \mu\text{m}$ height image of an individual growth spiral, recorded at a scan rate of 2.00 Hz.

potassium ferrocyanide crystal, to ensure that the electrode diffusion field did not intercept the sample. Assuming planar diffusion, the diffusion field length, δ , can be calculated from

$$\delta = \frac{nAFDc^*}{i_p} \quad (2)$$

where F is Faraday's constant, yielding a value of $\delta = 100\ \mu\text{m}$, using the experimental parameters quoted above.

Potassium Ferrocyanide Trihydrate (010) Surface Structure: Evidence for Growth Spirals. Figure 3a shows a typical AFM image of the (010) surface of potassium ferrocyanide trihydrate, recorded in air, after the crystal had been removed from the growth solution and dried quickly by carefully wicking away the excess solution with lens tissue. Although there is some precipitated material on the surface, which probably results from evaporation when the crystal is removed from the saturated solution, clearly evident are at least eight pyramidally shaped structures (labeled in Figure 3a). These features are not artifacts of the tip imaging process,²⁸ as higher resolution images, such as the one shown in Figure 3b, reveal the pyramidal structures to be spiral growth hillocks, providing evidence for the operation of the spiral BCF mechanism^{11,29} in the growth of potassium ferrocyanide trihydrate single crystals. This observation is not surprising given that classical BCF theory predicts that spiral growth at screw dislocations will dominate near equilibrium conditions.¹¹ Alternative growth mechanisms, such as the "birth

and spread" process,³⁰ which require a large supersaturation as a driving force, are strongly disfavored. Growth spirals have been observed for a variety of other single crystals, grown close to saturation, using interferometry,¹² ex situ,^{13–16} and in situ^{17–19} AFM. Figure 3a and other images recorded in different areas of the (010) crystal face, suggested a dislocation density of ca. $10^5\ \text{cm}^{-2}$.

The morphology of the growth spirals, in relation to the structure of the crystal lattice, is of particular interest. Figure 4 shows the projection of the potassium ferrocyanide trihydrate structure along the b axis, giving a top view of the (010) plane. The periodic bond chain (PBC) vector,^{29,31} which refers to the direction of lowest surface energy, corresponding to the strongest crystallographic bonding direction, occurs in the [201] and [102] directions.³² The repeat unit in the crystal lattice is formed from two (010) lattice planes shifted by $1/2a$, $1/2c$, with respect to one another, such that the N atoms of the vertical CN groups in the top layer (black outline) come exactly in the middle of the four potassium ions in the underlying layer (gray outline),³² as shown in Figure 4. The height image of the spiral growth hillock, in Figure 3b, depicts two steps emanating from the same dislocation core, separated by an interstep spacing (in the b direction) of $5 \pm 1\ \text{\AA}$, consistent with the unit cell dimensions. The lower layer is offset with respect to the upper layer, based on the crystal structure discussed above. As the spiral grows outward, the two layers appear to align along the most stable [201] and [102] crystallographic directions, giving step heights of $11 \pm 1\ \text{\AA}$, while they separate, at the intersection between the [201] and [102] directions, to give interleaved layers (step height $5 \pm 1\ \text{\AA}$).

IE-AFM Induced Dissolution. As noted above, the procedure adopted to electrically insulate the probe leaves the tip, the cantilever, and a small section of the underside of the AFM chip exposed to the solution. Before examining dissolution images, it is informative to consider the effective area over which the IE-AFM probe induces dissolution during a potential pulse. In general, dissolution will be induced only in areas where the diffusion field has intercepted the substrate. At the simplest level, assuming a planar diffusion profile, the *maximum* diffusion layer thickness is given by³³

$$\delta = \sqrt{D\pi t} \quad (3)$$

where t is the potential pulse length. For the saturated $\text{Fe}(\text{CN})_6^{4-}$ system, a pulse width of $t = 0.5\ \text{s}$, gives $\delta \approx 30\ \mu\text{m}$.

With the tip in contact with the surface, the separation of the cantilever from the underlying substrate varies from $3\ \mu\text{m}$, in the vicinity of the tip, to ca. $40\ \mu\text{m}$, where the lever attaches to the main body of the probe. The calculated value of δ thus suggests that only the cantilever and tip will be effective at electrochemically inducing dissolution. Even though part of the probe body may be exposed and electrochemically active, its role in the induced dissolution process is likely to be negligible, since the probe body–substrate separation exceeds the diffusion layer thickness. Moreover, this part of the probe is far removed from the region of the tip where images are obtained.

Previous SECM studies found the dissolution kinetics of the (010) surface of potassium ferrocyanide trihydrate to be very fast.²² The electrode–crystal surface separations ($3\text{--}40\ \mu\text{m}$), for the electroactive cantilever, are sufficiently large to ensure that the dissolution images reported below relate to effectively diffusion-controlled conditions, although it must be recognized that mass transport rates may vary over the region of interest due to the slope of the cantilever giving a change in the electrode–crystal separation. Directly under the tip, the electrode–

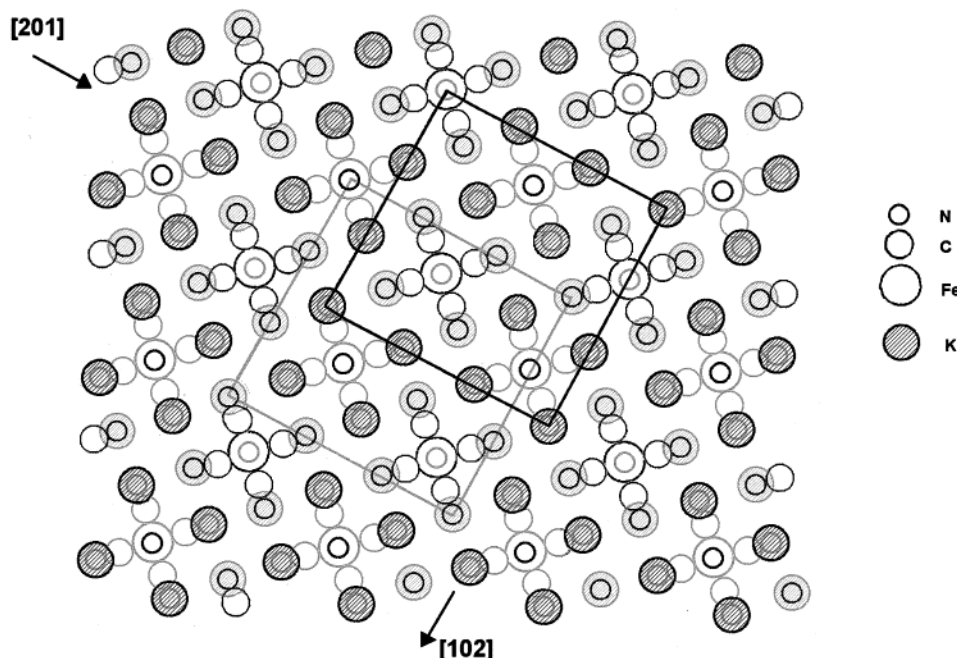


Figure 4. Projection of the potassium ferrocyanide trihydrate structure along the *b* axis, giving a top view of the (010) plane. The outlines of the atoms in the top layer are drawn in black, while the outlines of the atoms in the underlying layer are drawn in gray.

crystal separation is much smaller, and this tiny portion of the substrate may be subject to surface kinetic limitations. However, this area, primarily governed by the radius of the tip (20–60 nm), is minimal compared to the area of the crystal subjected to dissolution and imaged.

A potential problem in the earlier SECM studies²² was the buildup of the product of tip electrolysis, $\text{Fe}(\text{CN})_6^{3-}$, in the thin layer between the UME and the crystal surface. This was circumvented by the employment of short potential pulses (<1 s), an approach adopted for the studies described herein. Moreover, with the more open design of the IE-AFM probe,²⁵ compared to the UMEs used in the SECM-induced dissolution experiments,^{21–23} it is expected that $\text{Fe}(\text{CN})_6^{3-}$ produced at the tip and cantilever will diffuse away from the reaction zone more easily.

Figure 5 highlights the ability of the IE-AFM probe to electrochemically induce dissolution from the (010) surface of potassium ferrocyanide trihydrate. The tip was scanned from left to right (fast scan axis) and top to bottom (slow scan axis) at a scan speed of 6.1 Hz. The initial top half of the scan was recorded with the tip unbiased, and reflects the structure of the surface in contact with a saturated solution of $\text{Fe}(\text{CN})_6^{4-}$, which can be seen to be very flat. In this area, only three widely spaced steps (terrace width $6.0 \pm 0.3 \mu\text{m}$; step height $11 \pm 1 \text{ \AA}$) are observed. Halfway down the scan, with the tip in contact with the surface, the potential was pulsed from open circuit to +0.42 V (high mass transport rate: see Figure 2) for 0.5 s, and back to open circuit. This process serves to locally deplete $\text{Fe}(\text{CN})_6^{4-}$ adjacent to the crystal surface, thus providing the driving force for dissolution. The surface was observed to reconstruct, in response to the electrochemical perturbation, as evident from the lower half of the scan. The number of steps increased, with the interstep spacing decreasing (terrace width ca. $2 \pm 0.3 \mu\text{m}$; step height $15 \pm 1 \text{ \AA}$). As will be shown later, these steps are most likely to originate from dislocation sites.

Figures 6–9 show a sequence of in situ IE-AFM images of the same area of the (010) surface of potassium ferrocyanide trihydrate recorded prior to (Figure 6a) and after (Figures 6b–e, 7, 8, and 9) electrochemically inducing dissolution, at different

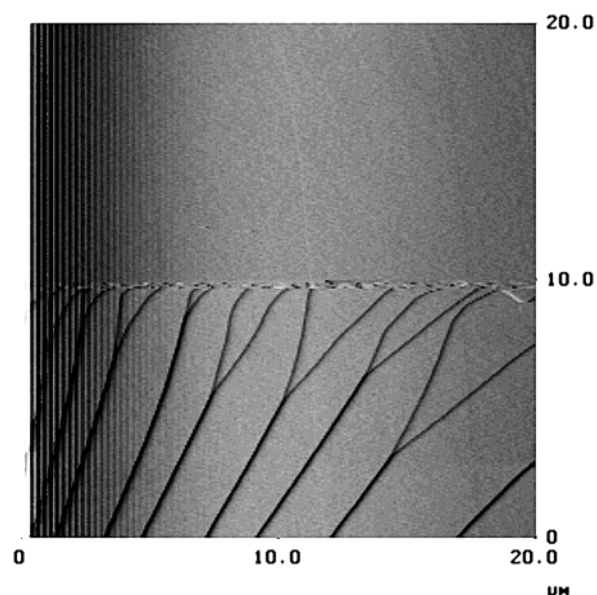


Figure 5. $20 \mu\text{m} \times 20 \mu\text{m}$ IE-AFM deflection image recorded at a scan rate of 6.10 Hz, demonstrating the immediate effect of electrochemically inducing the dissolution process. The tip was pulsed to +0.42 V for 0.5 s, halfway down the scan, with the tip in contact with the surface.

electrode driving potentials. In all cases, the probe potential was pulsed with the tip located in the center of the scan image and retracted $0.11 \mu\text{m}$ from the crystal. The surface was imaged as it returned to a state of equilibrium and the process was repeated by sequentially pulsing to increasingly positive electrode potentials. Although the images presented in these figures relate to one area of a specific crystal, the patterns of reactivity shown are typical of six crystal surfaces investigated.

For the images displayed collectively in Figure 6, the IE-AFM probe was pulsed from open circuit to +0.24 V (point A in Figure 2), for 0.5 s, and then back to open circuit. The step to +0.24 V is just into the $\text{Fe}(\text{CN})_6^{4-}$ oxidation wave, thus only slightly depleting the $\text{Fe}(\text{CN})_6^{4-}$ concentration in the probe–substrate gap, and providing a small driving force (diffusion

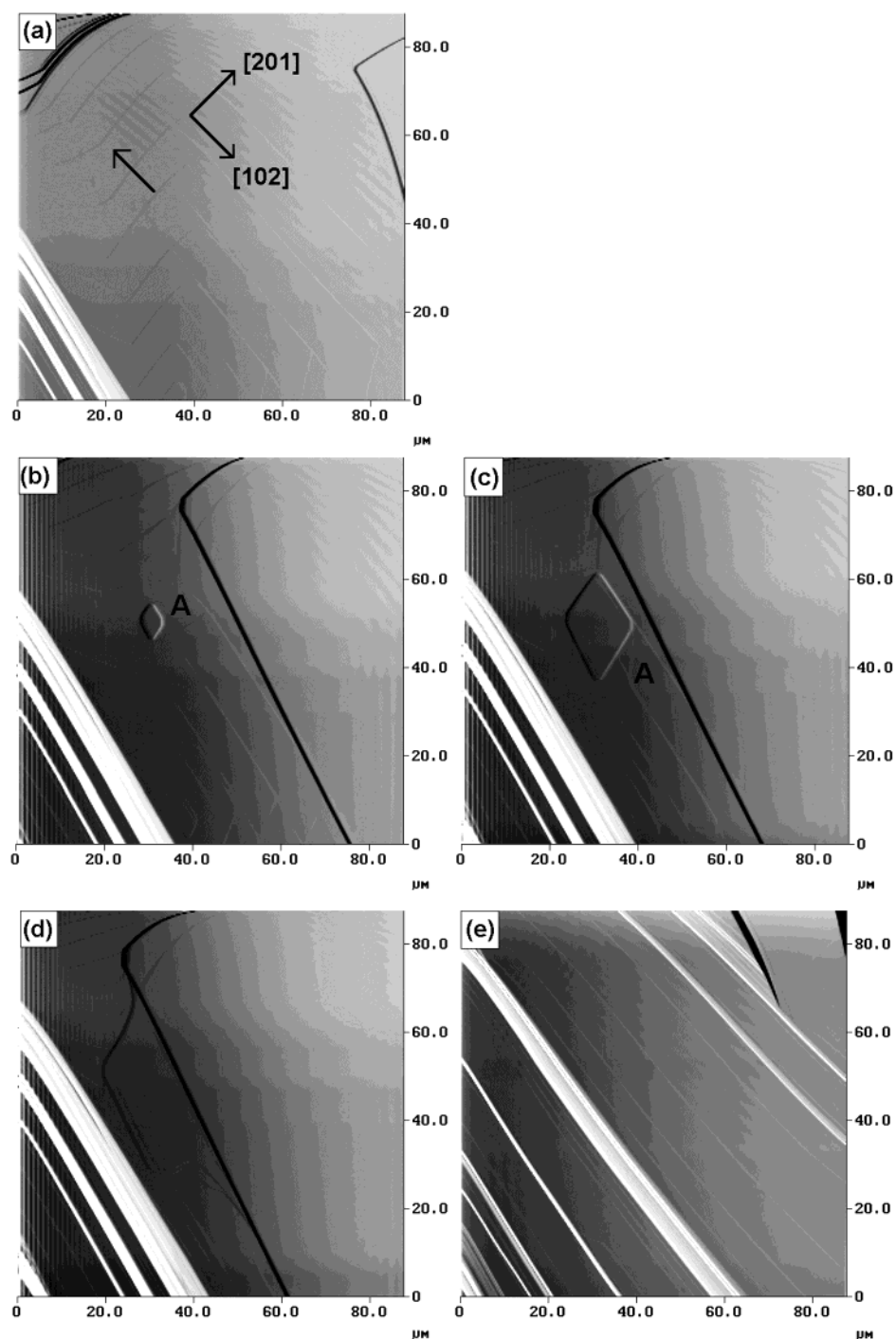


Figure 6. $87.7\ \mu\text{m} \times 87.7\ \mu\text{m}$ IE-AFM deflection images recorded at a scan rate of 6.1 Hz: (a) prior to electrochemical induction of the dissolution process; (b–e) after inducing the dissolution process. The tip potential was pulsed to +0.24 V for 0.5 s and the image recorded at times of (b) 42 s, (c) 84 s, (d) 126 s, and (e) 12 min after the initial potential pulse.

gradient) to promote dissolution. Figure 6a, recorded prior to initiating dissolution, clearly shows part of a dissolution spiral. A very slowly dissolving surface is not unexpected under saturated solution conditions, since small temperature increases in the fluid cell can arise from the diode laser in the detection unit.^{25,34} The associated steps of the dissolution spiral are aligned along the [201] and [102] directions, which were found to dominate in the growth spirals. To the left of the image, the steps along the [201] direction appear to break, as indicated by the arrow, almost running parallel to the [102] direction, signifying, perhaps, the site of an underlying defect site. It is in this area that an etch pit is seen to open up after depleting

ferrocyanide in the solution above the crystal surface (Figure 6b).

An image of the surface, 42 s after electrochemically inducing dissolution, is shown in Figure 6b. The predominant dissolution activity, under the low driving conditions employed, appears to come from preexisting steps, aligned in the [102] direction, which move from the bottom right and top left-hand corners toward the center of the image. The spiral at the bottom of the image has continued to dissolve, but at a faster rate compared with initial conditions (Figure 6a), as indicated by the decrease in the interstep spacing. Additional dissolution activity has resulted in the formation of a diamond-shaped shallow (ca. 63

Å deep) etch pit (labeled A). The morphology of this pit can be related to the structure of the (010) surface, with the outline showing strong preference for the [201] and [102] directions.

Figure 6c shows that 42 s later, the crystal surface has continued to dissolve, to ensure that the solution returns to equilibrium. The dominant step in the left of the image has moved even further to the right, while the etch pit has increased in size. The advancing steps from the bottom right of the image have moved across the dislocation site, indicating that under these driving force conditions, the rate at which steps retreat along the [102] direction occurs faster than the rate at which spiral dislocation sites unwind. This has the effect that spiral development appears to be suppressed in areas where the retreating steps encounter a dislocation site. After a further 42 s, the etch pit is no longer visible and dissolution continues to be dominated by step movement (Figure 6d). Over a period of 12 min, the surface was observed to return to a fairly static state (Figure 6e).

The evolving topography of the surface after a 0.5 s potential pulse further into the $\text{Fe}(\text{CN})_6^{4-}$ oxidation wave, from open circuit to +0.29 V (point B in Figure 2) and then back to open circuit, is shown in Figure 7. Under these higher driving force conditions, dissolution still occurs predominantly by the movement of preexisting steps, accompanied by the nucleation and growth of several etch pits. The image in Figure 7a, recorded 42 s after the potential pulse, shows the nucleation of a new etch pit (labeled B) on the right edge of the image, with a morphology again determined by the dominant crystallographic axes. The area where etch pit A was revealed previously shows only a small hole (ca. $0.8\ \mu\text{m}$ in diameter), again providing evidence for the location of a defect site in this area. The preferential growth of etch pit B over A at higher driving force suggests a difference in the activity of the two regions during dissolution. The large difference in activity cannot be explained by a variation in the mass transport rate since this is expected to be highest in the center of the image where the tip was located during the potential pulse, decreasing on moving outward from this point. The suppressed development of pit A is likely to be due to the fact that it is now located in a region of high step density, which provides the dominant source of material for dissolution.

With time, etch pit B continues to expand and deepen slightly (Figure 7b). Of particular interest is the observation of steps, of height $5 \pm 1\ \text{\AA}$, inside the pit. These show the same interleaved layer structure, where the [201] and [102] crystallographic directions intersect, as observed in the growth spiral. This suggests that under conditions where the crystal–solution interface remains close to saturation (due to the rapid dissolution kinetics of this surface), etch pits on the (010) surface of potassium ferrocyanide trihydrate nucleate at the sites of screw dislocations. Pit formation appears to involve the unwinding of steps which orientate along the directions indicated, ultimately resulting in macroscopic-sized etch pits. Although there have been several studies of etch pit formation at dislocations,^{7,13,29,35} this investigation represents the first, real time, in situ evidence for the operation of the spiral dissolution mechanism in the formation of pits. Further evidence that this is the mechanism of pitting is provided below. At this stage of the dissolution process another pit (labeled C), adjacent to etch pit B, is evident. The small hole (A) has decreased in width and depth.

Figure 7c depicts the surface 126 s after application of the initial potential pulse. Dissolution from etch pit B and the movement of steps from the left are clearly the dominant dissolution processes, as the surface returns to equilibrium.

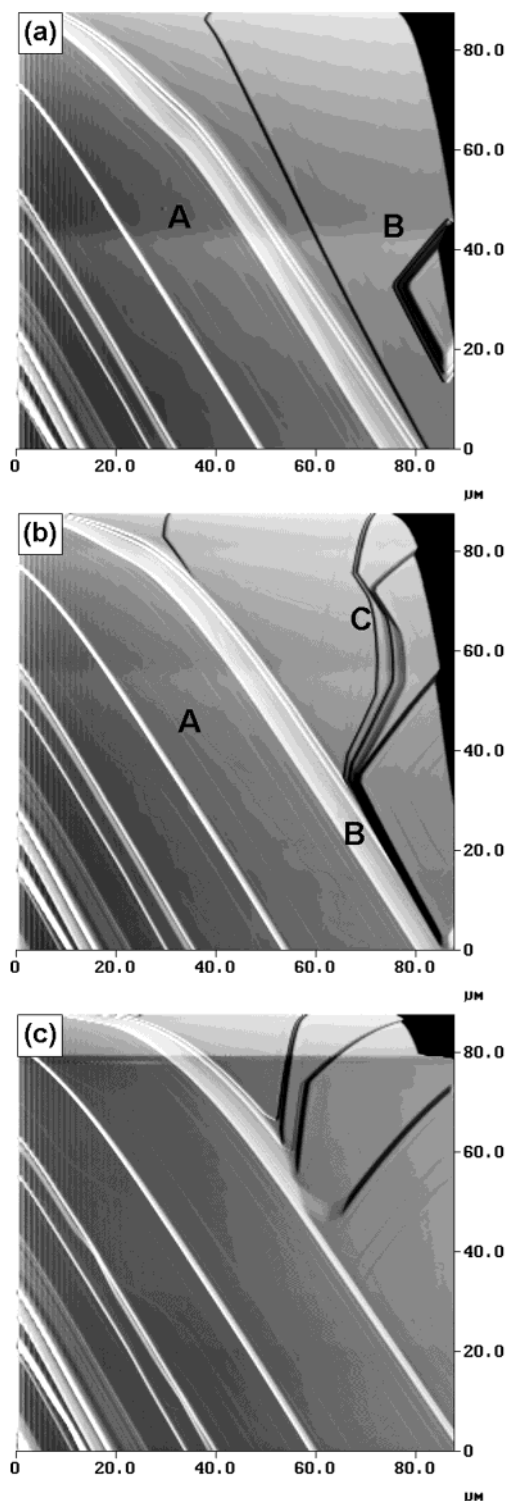


Figure 7. $87.7\ \mu\text{m} \times 87.7\ \mu\text{m}$ IE-AFM deflection images recorded at a scan rate of 6.1 Hz: (a) 42 s after, (b) 84 s after, and (c) 126 s after electrochemically inducing dissolution by pulsing the probe to +0.29 V for 0.5 s.

To further increase the transport driving force exerted on the dissolution process, the potential of the probe was pulsed from open circuit to +0.33 V for 0.5 s and then back to open circuit. This potential corresponds to a position close to the top of the $\text{Fe}(\text{CN})_6^{4-}$ oxidation wave (point C in Figure 2). Figure 8a shows the crystal surface 42 s after electrochemically inducing dissolution. Of immediate note is the increased rate of dissolution of the surface. The density of steps, aligned in the dominant [102] direction, has significantly increased. At this potential,

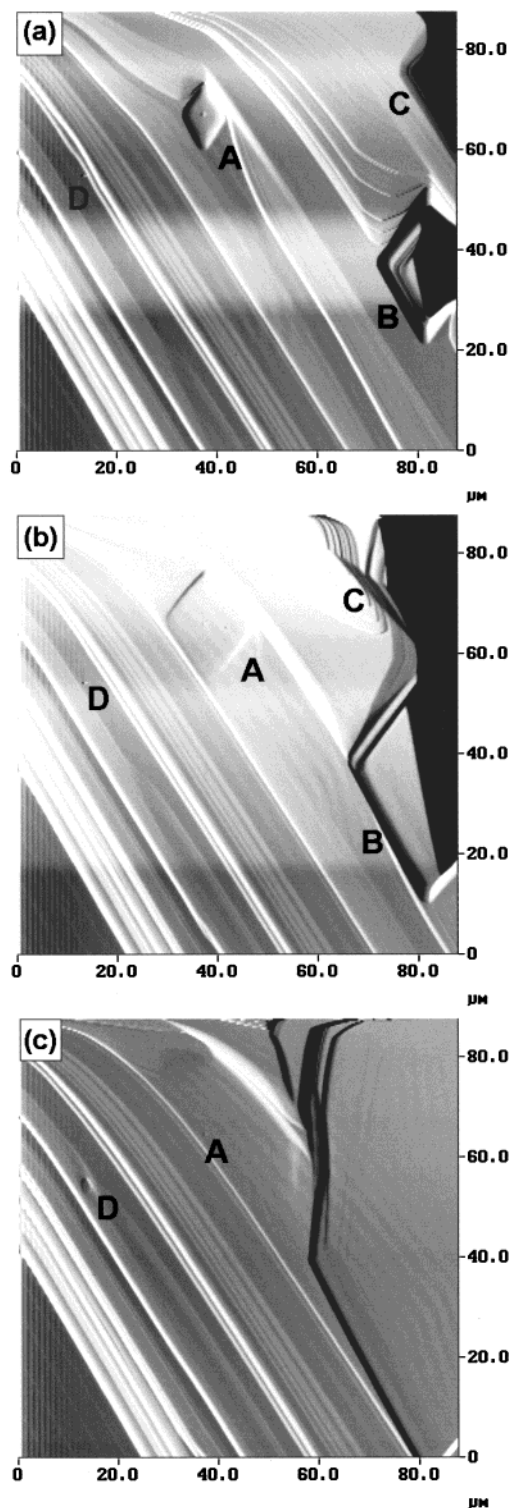


Figure 8. $87.7 \mu\text{m} \times 87.7 \mu\text{m}$ IE-AFM deflection images recorded at a scan rate of 6.1 Hz: (a) 42 s after, (b) 84 s after, and (c) 126 s after electrochemically inducing dissolution by pulsing the probe to +0.33 V for 0.5 s.

the transport driving force is large enough to reveal etch pits A, B, and C and a small hole, ca. $0.7 \mu\text{m}$ in diameter, labeled D. It will be shown later that this defect marks the site of a screw dislocation, which is only revealed at a higher dissolution driving force (Figure 9). Interestingly, if the dimensions of etch pit B recorded at approximately the same time after application of the potential pulse, under different driving force conditions (Figures 7a and 8a) are compared, we find that the width and length of the pit remain constant but the depth has increased

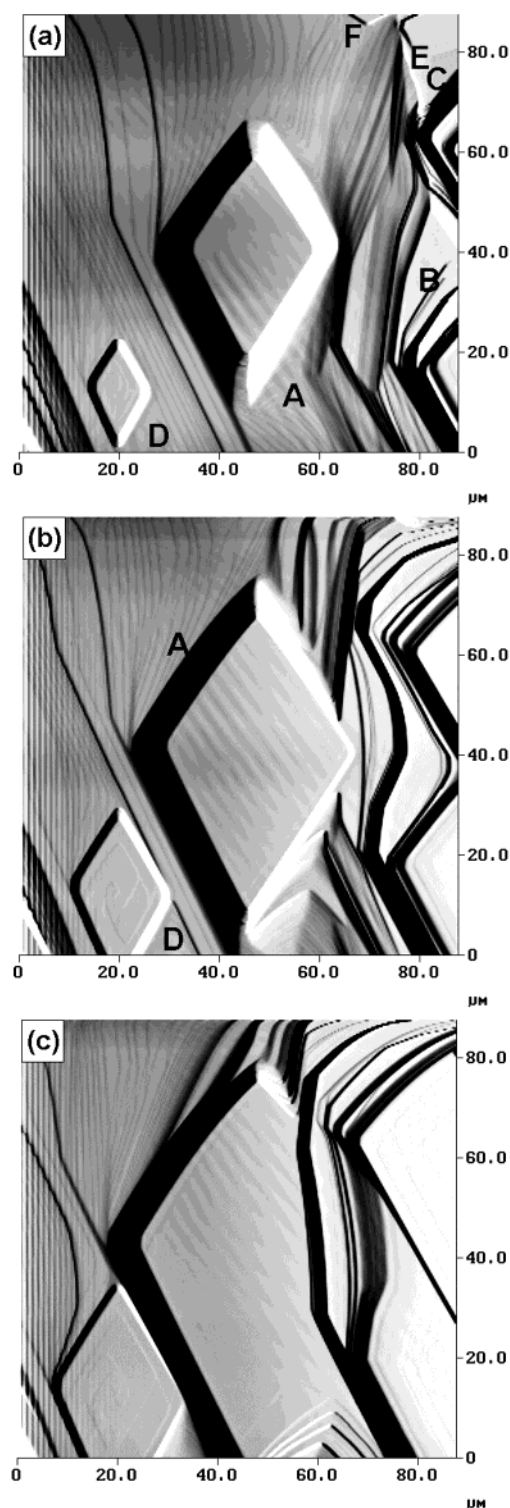


Figure 9. $87.7 \mu\text{m} \times 87.7 \mu\text{m}$ IE-AFM deflection images recorded at a scan rate of 6.1 Hz: (a) 42 s after, (b) 84 s after, and (c) 126 s after electrochemically inducing dissolution by pulsing the probe to +0.36 V for 0.5 s.

significantly, from 105 nm (Figure 7a) to 175 nm (Figure 8a). This suggests that, for this particular pit, the rate of removal of material from the core of the defect, in a direction normal to the surface, increases with increased driving force, while the radial retreat of steps is effectively independent of driving force.

The subsequent image, recorded 84 s after application of the potential pulse (Figure 8b), shows the dissolution rate of the surface slowing, as the system returns to equilibrium. The interstep spacing has, in general, increased and the etch pits

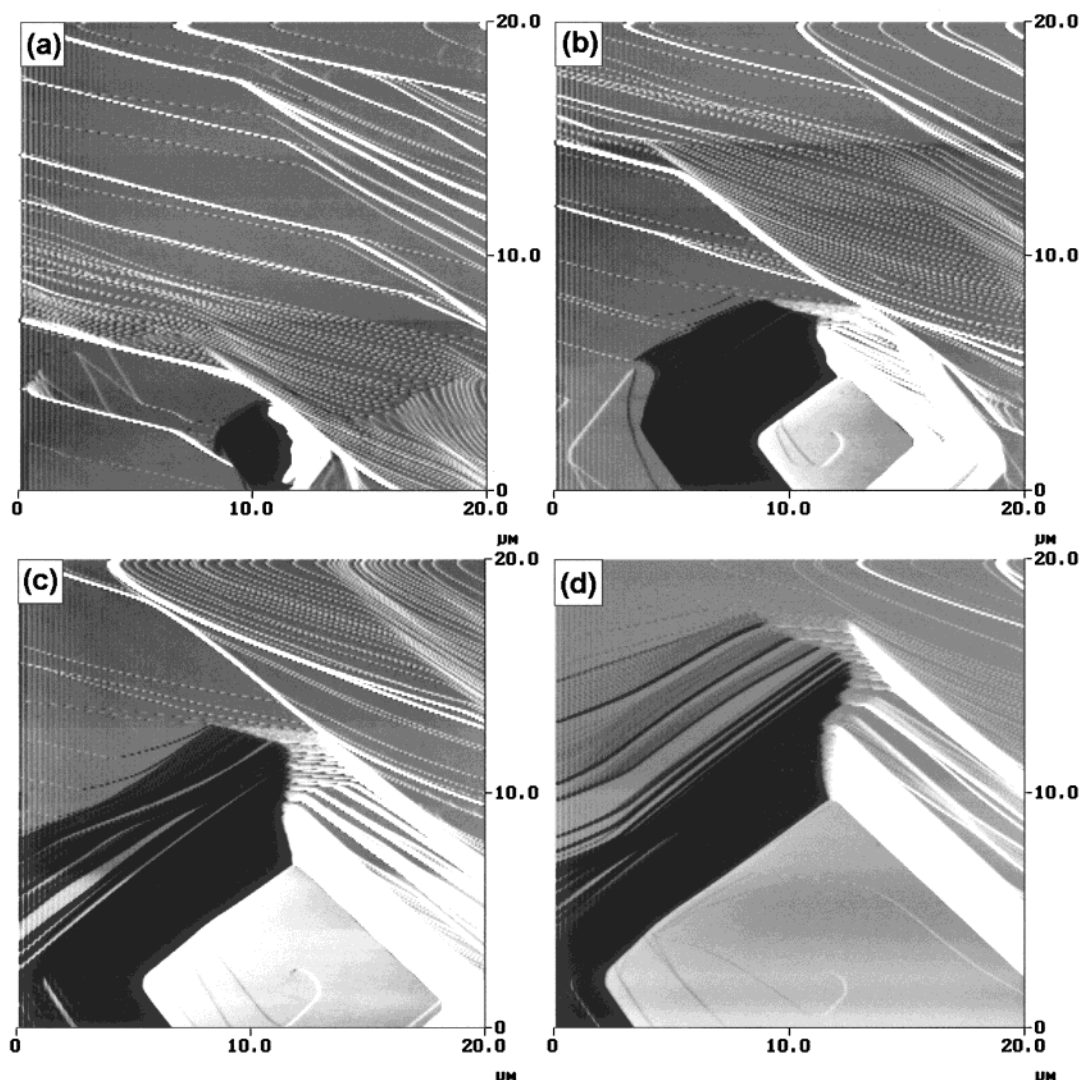


Figure 10. $20\ \mu\text{m} \times 20\ \mu\text{m}$ IE-AFM deflection images recorded at a scan rate of 6.1 Hz: (a) 90 s after, (b) 216 s after, (c) 258 s after, and (d) 300 s after electrochemically inducing dissolution by pulsing the probe to +0.34 V for 0.5 s, with the tip positioned over a dislocation site.

have continued to open out as the steps retreat, except at site D which appears to be relatively inactive to dissolution. After a further 42 s, the surface topography is as depicted in Figure 8c. Site D has now become activated, increasing in diameter as material is removed from this area by dissolution. This switch in dissolution activity could possibly be attributed to the interaction between neighboring sites, which compete to provide material to the solution through dissolution. Initially the most active sites dissolve, locally saturating the solution and thus reducing the driving force for the dissolution of neighboring sites. As dissolution proceeds, and the rate of dissolution at the most active sites slows, sites which were previously inactive can become active if there is a local undersaturation. Similar types of effect have been observed between closely spaced redox active sites on the surface of Ta/Ta₂O₅,³⁶ under conditions where the sites compete for the same reactant molecules.

To provide the maximum transport driving force, the probe was pulsed from open circuit to +0.36 V (point D in Figure 2) for 0.5 s and then back to open circuit. Under these conditions, six etch pits (labeled A–F) were revealed in total (Figure 9a, recorded 42 s after the application of the potential pulse). Of the six, pits A, B, and C were observed at the lower driving forces (but were much shallower), while the presence of site D was suggested by the appearance of a small dissolution hole, in Figure 8. The two previously unobserved nucleation sites, E

and F, are located just in the top right-hand corner of the image. With the extensive dissolution activity generated at this driving potential, the images depicted in Figure 9 have been shifted slightly downward by ca. 10–15 μm to those previously recorded in Figures 6–8, enabling nucleation sites E and F to be revealed. The etch pit density suggested by this image and others recorded in different areas of the crystal face under identical experimental conditions, $0.8 (\pm 0.2) \times 10^5$ dislocations cm^{-2} , correlates well with the growth hillock density observed in Figure 3a, suggesting that etch pits nucleate at the site of spiral growth hillocks.^{29,35,37,38} At this higher driving force, pitting is seen to provide the dominant dissolution pathway, although there is still some movement of preexisting steps.

The larger dimensions of etch pit A (length 57.1 μm ; width 30.4 μm ; depth 360 nm) compared to D (length 21.8 μm ; width 12.3 μm ; depth 96 nm) tentatively suggest that site A is initially more active than D. Inside etch pit D, steps winding down to a dislocation core are clearly observed, providing more evidence for the screw dislocation mechanism in dissolution from the (010) surface of potassium ferrocyanide trihydrate. As expected, based on the crystal morphology discussed above, two step layers emerge from the same core point, one after the other, with step heights of $5 \pm 1\ \text{\AA}$. The strong interference fringes present in the image, arising from the high reflectivity of the crystal surface causing interference on the optical signal, make

it difficult to determine whether steps emerging from a spiral dislocation are present in etch pit A.

After a further 42 s (Figure 9b) and 84 s (Figure 9c) dissolution proceeds toward a state of equilibrium, primarily by the continued expansion of etch pits. The general characteristics of the spiral at the base of etch pit D, in both parts b and c of Figure 9, are consistent with those observed on the spiral growth hillock (Figure 3a), i.e., step layers align along the dominant [201] and [102] crystallographic directions but separate where these axes intersect. The interstep spacing associated with the spiral steps, in etch pit D, increase in size over the course of 84 s, as the dissolution rate slows and the surface returns to equilibrium.

In general, under low transport driving forces, dissolution proceeds primarily by the movement of preexisting steps (Figure 6). However, as the transport driving conditions are increased, this route is unable to supply all of the material to maintain the crystal surface close to saturated conditions. The dominant dissolution mechanism becomes the opening of diamond-shaped etch pits by the unwinding of steps associated with screw dislocations (Figures 7–9). This mechanism is further confirmed by the results presented in Figure 10, which show a sequence of AFM images recorded 90 s (Figure 10a), 216 s (Figure 10b), 258 s (Figure 10c), and 400 s (Figure 10d) after the probe had been used to electrochemically induce dissolution. In this case, dissolution was induced with the tip located over, and in contact with, a preexisting dislocation site, with the potential pulsed from open circuit to +0.34 V for 0.5 s and then back to open circuit. Figure 10a shows the presence of a deep etch pit, with a spiral located at the center. Over the subsequent period, the surface continues to slowly dissolve, via the pit opening out as steps associated with the spiral retreat by unwinding.

Conclusions

The integrated electrochemical–AFM has allowed the surface processes that accompany dissolution from the (010) surface of potassium ferrocyanide trihydrate in aqueous solution to be monitored in real time. Under low transport driving force conditions, the dissolution process proceeds primarily by the retreat of preexisting steps, aligned in the [102] crystallographic direction. As the driving force is increased, by increasing the potential applied to the IE-AFM probe, dissolution occurs by the unwinding of steps from screw dislocations. This mechanism leads to the formation of etch pits, whose morphology is determined by the dominant [201] and [102] crystallographic axes. The observed surface dynamics are consistent with classical dissolution models and earlier SECM kinetic studies.

Although studies of the effect of driving force on dissolution with the IE-AFM are largely qualitative, work is planned to model mass transport in the zone between the probe and the substrate of interest. This should enable the current measured at the electrode to be correlated with interfacial reactivity and allow the driving force for dissolution (undersaturation) to be predicted quantitatively.

Acknowledgment. J.V.M. and C.J.E. thank the EPSRC (ROPA:GR/L71377) and Unilever Research, Port Sunlight Laboratory (Dental Division), respectively, for support. We are grateful to Dr. Zoe H. Barber (Department of Materials Science and Metallurgy, University of Cambridge) for platinum coating the AFM tips used in this study.

References and Notes

- (1) Macpherson, J. V.; Unwin, P. R. *Prog. React. Kinet.* **1995**, *20*, 185.
- (2) Unwin, P. R.; Macpherson, J. V. *Chem. Soc. Rev.* **1995**, *24*, 109.
- (3) Stumm, W., Ed. *Aquatic Surface Chemistry*; Wiley: New York, 1989.
- (4) Heimann, R. B. *Crystals: Growth, Properties and Applications*; Springer-Verlag: Berlin, 1982.
- (5) Nancollas, G. H., Ed. *Biological Mineralisation and Demineralisation*; Springer-Verlag: Berlin, 1982.
- (6) See for example: (a) Weisendanger, R. *Scanning Probe Microscopy and Spectroscopy*; Cambridge University Press: Cambridge, UK, 1994. (b) Synder, S. R.; White, H. S. *Anal. Chem.* **1992**, *64*, R166.
- (7) Gratz, A. J.; Manne, S.; Hansma, P. K. *Science* **1991**, *251*, 1343.
- (8) Malkin, A. J.; Kuznetsov, Yu. G.; McPherson, A. J. *Struct. Biol.* **1996**, *117*, 124.
- (9) Bosbach, D.; Rammensee, W. *Geochim. Cosmochim. Acta* **1994**, *58*, 843.
- (10) Tiller, W. A. *The Science of Crystallisation: Microscopic Interfacial Phenomena*; Cambridge University Press: New York, 1991.
- (11) Burton, W. K.; Cabrera, N.; Frank, F. C. *Philos. Trans. R. Soc. London* **1951**, *A243*, 299.
- (12) (a) Van der Hoek, B.; Letten, L. A. M.; Enkevort, W. J. P. *J. Cryst. Growth* **1983**, *62*, 603. (b) Tsukamoto, K. *J. Cryst. Growth* **1983**, *61*, 199.
- (13) Sangwal, K.; Servat, J.; Sanz, F.; Torrent-Burgués, J. *J. Cryst. Growth* **1997**, *180*, 263.
- (14) Shindo, H.; Shitagami, K.; Kondo, S.; Seo, A. *J. Cryst. Growth* **1999**, *198*, 253.
- (15) (a) Ester, G. R.; Price, R.; Halfpenny, P. J. *J. Cryst. Growth* **1997**, *182*, 95. (b) Ester, G. R.; Price, R.; Halfpenny, P. J. *J. Phys. D: Appl. Phys.* **1999**, *32*, A128.
- (16) Maiwa, K.; Plomp, M.; Van Enckervort, W. J. P.; Bennema, P. *J. Cryst. Growth* **1998**, *186*, 214.
- (17) Land, T.; De Yereo, J. J.; Lee, J. D. *Surf. Sci.* **1997**, *384*, 136.
- (18) Pina, C. M.; Becker, U.; Risthaus, P.; Bosbach, D.; Putnis, A. *Nature* **1998**, *395*, 483. (b) Bosbach, D.; Hall, C.; Putnis, A. *Chem. Geol.* **1998**, *151*, 143.
- (19) Gratz, A. J.; Hillner, P. E.; Hansma, P. K. *Geochim. Cosmochim. Acta* **1993**, *57*, 491.
- (20) For reviews see for example: (a) Bard, A. J.; Fan, F.-R. F.; Pierce, D. T.; Unwin, P. R.; Wipf, D. O.; Zhou, F. *Science* **1991**, *254*, 68. (b) Bard, A. J.; Fan, F.-R. F.; Mirkin, M. V. In *Electroanalytical Chemistry*; Bard, A. J., Ed.; Marcel Dekker: New York, 1994; Vol. 18, pp 243–373. (c) Mirkin, M. V. *Anal. Chem.* **1996**, *68*, A177. (d) Barker, A. L.; Gonsalves, M.; Macpherson, J. V.; Slevin, C. J.; Unwin, P. R. *Anal. Chim. Acta* **1999**, *385*, 223.
- (21) (a) Macpherson, J. V.; Unwin, P. R. *J. Chem. Soc., Faraday Trans.* **1993**, *89*, 1883. (b) Macpherson, J. V.; Unwin, P. R. *J. Phys. Chem.* **1994**, *98*, 1704. (c) Macpherson, J. V.; Unwin, P. R. *J. Phys. Chem.* **1994**, *98*, 3109.
- (22) Macpherson, J. V.; Unwin, P. R. *J. Phys. Chem.* **1995**, *99*, 3338.
- (23) (a) Macpherson, J. V.; Unwin, P. R. *J. Phys. Chem.* **1995**, *99*, 14824. (b) Macpherson, J. V.; Unwin, P. R. *J. Phys. Chem.* **1996**, *100*, 19475.
- (24) Kwak, J.; Bard, A. J. *Anal. Chem.* **1989**, *61*, 1221.
- (25) Macpherson, J. V.; Hillier, A. C.; Unwin, P. R.; Bard, A. J. *J. Am. Chem. Soc.* **1996**, *118*, 6445.
- (26) Jones, C. E.; Macpherson, J. V.; Barber, Z. H.; Somekh, R. E.; Unwin, P. R. *Electrochem. Commun.* **1999**, *1*, 55.
- (27) Bard, A. J.; Faulkner, L. R. *Electrochemical Methods*; John Wiley: New York, 1980; p 218.
- (28) (a) Grutter, P.; Zimmermann, W.; Brodbeck, D. *Appl. Phys. Lett.* **1992**, *60*, 2741. (b) Jarausch, K. F.; Stark, T. J.; Russell, P. E. *J. Vac. Sci. Technol. B* **1996**, *14*, 3425.
- (29) Sangwal, K. *Etching of Crystals: Theory, Experiment and Application*; North-Holland: Amsterdam, 1987.
- (30) (a) Ohara, M.; Reid, R. C. *Modeling Crystal Growth Rates from Solution*; Prentice Hall: Englewood Cliffs, NJ, 1973, and references therein; (b) Bennema, P. *J. Cryst. Growth* **1984**, *69*, 182.
- (31) (a) Hartmann, P.; Perdok, W. *Acta Crystallogr.* **1955**, *8*, 49, 521, 525. (b) Hartmann, P. In *Crystal Growth—An Introduction*; Hartmann, P., Ed.; North-Holland: Amsterdam, 1973; p 367.
- (32) Donnay, J. D. H.; Ondik, H. M. Eds. *Inorganic Compounds*; National Bureau of Standards: Washington, DC, 1973; Vol 2, pp 421–424.
- (33) Brett, C. M. A.; Brett, A. M. O. *Electrochemistry, Principles, Methods and Applications*; Oxford University Press: Oxford, UK, 1996; p 95.
- (34) Kipp, S.; Lacmann, R.; Schneeweiss, M. A. *Ultramicroscopy* **1995**, *57*, 333.
- (35) Onuma, K.; Tsukamoto, K.; Sunagawa, I. *J. Cryst. Growth* **1991**, *110*, 724.
- (36) Basame, S. B.; White, H. S. *Anal. Chem.* **1999**, *71*, 3166.
- (37) Durbin, S. D.; Carlson, W. E.; Saros, M. T. *J. Phys. D: Appl. Phys.* **1993**, *26*, B128.
- (38) Vekilov, P. G.; Kuznetsov, Yu. G.; Chernov, A. A. *J. Cryst. Growth* **1990**, *102*, 706.